



Cryo-ET of *Toxoplasma* parasites gives subnanometer insight into tubulin-based structures

Stella Y. Sun^{a,1}, Li-av Segev-Zarko^{b,1}, Muyuan Chen^{c,1}, Grigore D. Pintilie^a, Michael F. Schmid^d, Steven J. Ludtke^{c,e}, John C. Boothroyd^{b,2}, and Wah Chiu^{a,b,d,2}

^aDepartment of Bioengineering, James H. Clark Center, Stanford University, Stanford, CA 94305; ^bDepartment of Microbiology and Immunology, Stanford University School of Medicine, Stanford, CA 94305; ^cVerna Marrs and McLean Department of Biochemistry and Molecular Biology, Baylor College of Medicine, Houston, TX 77030; ^dDivision of CryoEM and Bioimaging, SSRL, SLAC National Accelerator Laboratory, Stanford University, Menlo Park, CA 94025; and ^eCryo-EM Core, Baylor College of Medicine, Houston, TX 77030

Edited by J. McIntosh, Department of Molecular, Cellular and Developmental Biology, University of Colorado Boulder, Boulder, CO; received June 24, 2021; accepted December 29, 2021

Tubulin is a conserved protein that polymerizes into different forms of filamentous structures in *Toxoplasma gondii*, an obligate intracellular parasite in the phylum Apicomplexa. Two key tubulin-containing cytoskeletal components are subpellicular microtubules (SPMTs) and conoid fibrils (CFs). The SPMTs help maintain shape and gliding motility, while the CFs are implicated in invasion. Here, we use cryogenic electron tomography to determine the molecular structures of the SPMTs and CFs in vitrified intact and detergent-extracted parasites. Subvolume densities from detergent-extracted parasites yielded averaged density maps at subnanometer resolutions, and these were related back to their architecture in situ. An intraluminal spiral lines the interior of the 13-protofilament SPMTs, revealing a preferred orientation of these microtubules relative to the parasite's long axis. Each CF is composed of nine tubulin protofilaments that display a comma-shaped cross-section, plus additional associated components. Conoid protrusion, a crucial step in invasion, is associated with an altered pitch of each CF. The use of basic building blocks of protofilaments and different accessory proteins in one organism illustrates the versatility of tubulin to form two distinct types of assemblies, SPMTs and CFs.

that α - and β -tubulin proteins are expressed in *Toxoplasma* (13, 14), and a novel tubulin polymer in the conoid has been observed in detergent-extracted parasites (5). The precise molecular organization of tubulins in the apical complex and pellicle remained unclear, making it difficult to study how they interact and function during infection.

Cryogenic electron tomography (cryo-ET) is a powerful tool to study molecular structure in situ (15–18). This method can define the spatial context of cellular architecture without using chemical fixatives or metal stains. *Toxoplasma* tachyzoites are crescent shaped and ~ 2 by $6 \mu\text{m}$. Although these cells are generally too thick for the entire intact parasite to be studied by cryo-ET, our interest is in the tapered apical region, which is about 400 nm thick, thin enough for a 200- to 300-kV electron beam to form images. In this study, we focused on detailed image analysis of the subpellicular microtubules (SPMTs) and conoid fibrils (CFs) in intact parasites. In addition, we used detergent to remove the membranes and soluble components, leaving the insoluble cytoskeleton. This has the effect of making the specimen thinner overall and removing other obscuring

cryo-electron tomography | subtomogram averaging | tubulin | cytoskeleton | *Toxoplasma gondii*

Toxoplasma gondii belongs to the phylum Apicomplexa, which consists of a diverse group of obligate intracellular parasites. This single-celled eukaryote possesses a broad host range, capable of infecting almost any nucleated cell in any warm-blooded animal (1). Symptoms associated with *Toxoplasma* infection are diverse, ranging from mild to fatal, especially in the developing fetus or immunocompromised patients (e.g., those with AIDS, heart transplants, etc.). Because of its prevalence worldwide, *Toxoplasma* presents a global health problem.

Upon infection, tachyzoites, which are the rapidly growing, asexual forms of *Toxoplasma*, proliferate within the host cell and eventually cause host cell lysis. Released free tachyzoites are highly motile, actively invading more host cells. To accomplish this, they deploy a sophisticated and complex strategy involving a specialized, apical architecture and tightly choreographed secretion from two distinct secretory organelles: micronemes and rhoptries (2–4). Among the events associated with invasion is rearrangement of the cytoskeleton at the apical end, including protrusion of the conoid, a prominent bundle of spirally organized fibers (5–8).

The tubulin-based cytoskeleton that forms the pellicle and apical complex of *Toxoplasma* is not only responsible for cellular structural integrity but also provides a scaffold for cell motility and a polarized discharge of key invasion factors (9, 10). These crucial roles make these tubulin-based assemblies, including their interacting nontubulin partners, attractive drug targets for treating infection (11, 12). Proteomic analysis of a detergent-insoluble tachyzoite cytoskeleton fraction indicates

Significance

Tubulin polymers are essential for a variety of cellular functions. Using cryo-ET, we reveal the 3D organization of the apical complex in *Toxoplasma gondii*, an intracellular eukaryote with tubulin-based structures, including an apical “conoid” involved in host cell invasion. Our development of an advanced subtomogram averaging protocol for filamentous structures enabled us to accurately assign tubulins in cellular context. At the subnanometer resolution achieved, tubulins were confirmed to assemble into two major forms: canonical subpellicular microtubules (SPMTs) and noncanonical conoid fibrils (CFs). The data further revealed associated proteins in both structures, a dominant orientation of SPMTs, and a unique patterning of the CFs. This work demonstrates an approach that can be used to determine cellular filamentous structures at multiscale resolutions.

Author contributions: S.Y.S., L.S.-Z., M.C., J.C.B., and W.C. designed research; S.Y.S., L.S.-Z., M.C., G.D.P., M.F.S., and S.J.L. performed research; S.Y.S., L.S.-Z., M.C., G.D.P., and S.J.L. contributed new reagents/analytic tools; S.Y.S., L.S.-Z., M.C., G.D.P., M.F.S., S.J.L., J.C.B., and W.C. analyzed data; and S.Y.S., L.S.-Z., M.C., G.D.P., M.F.S., J.C.B., and W.C. wrote the paper.

The authors declare no competing interest.

This article is a PNAS Direct Submission.

This open access article is distributed under [Creative Commons Attribution-NonCommercial-NoDerivatives License 4.0 \(CC BY-NC-ND\)](https://creativecommons.org/licenses/by-nc-nd/4.0/).

¹S.Y.S., L.S.-Z., and M.C. contributed equally.

²To whom correspondence may be addressed. Email: jboothr@stanford.edu or wahc@stanford.edu.

This article contains supporting information online at <http://www.pnas.org/lookup/suppl/doi:10.1073/pnas.2111661119/-DCSupplemental>.

Published February 4, 2022.

cellular components. Subtomogram averaging was subsequently used for cytoskeleton components in both intact and detergent-extracted cells. Our analysis revealed unexpected structural differences in the tubulin protofilament organization of SPMTs and CFs at subnanometer resolution and enabled detection of their specific association with additional, yet-to-be-identified molecular components. Dissection of the components in apical complexes containing CFs and pellicles containing SPMTs provides a detailed understanding of how different tubulin-based macromolecular complexes are assembled in a cellular context and provides clues to their crucial roles in parasite biology.

Results

Cryo-ET Reveals Structural Details in the Apical Region of *Toxoplasma*. CFs and SPMTs are two types of tubulin-based cytoskeletal elements that maintain the shape and polarity of the apical complex and pellicle, which are key parts of the invasion machinery in *Toxoplasma*. Under calcium flux, a chemical stimulus critical to the invasion process in this phylum of parasites, the CFs protrude from the surrounding SPMTs (19), making the apical end of the parasites fall well within the thickness limitation of cryo-ET imaging (~500 nm). Using phase optical microscopy, we assessed the percentage of extracellular parasites exhibiting CF protrusion following calcium ionophore (A23187) treatment. Examination of tachyzoites before loading them on the EM grid showed ~87% presented a protruded conoid, ensuring a large number of parasites suitable for imaging. To maximize the recognition of distinct subcellular components in this structurally complex area of the cell, we used a Volta phase plate (VPP) located in the focal plane of the objective lens of the electron microscope (20). The resulting enhancement of image contrast facilitates the use of convolutional neural networks (15) for annotation of distinct secretory organelles and cytoskeleton elements in the apical region. Fig. 1 and *SI Appendix, Movie S1* show data for a representative tomogram generated in this way. Among the features revealed were the tubulin-based CFs and intraconoidal microtubules, bounded by two distinct preconoidal rings (PCRs) on top and the apical polar ring (APR) on the bottom, with micronemes, rhoptries, and other

organelles filling the conoid's interior space (Fig. 1 *B* and *E*). The SPMTs were aligned to the inner surface of the pellicle along the entire extent of the cell body apparent in our field of view. For tachyzoites presenting intermediate or completely retracted conoids, we can capture the retracted conoid shielded by the ring of SPMTs.

Transverse slices of the CF from the reconstructed tomograms exhibit a comma shape, consistent with previous negative staining electron microscopy studies (5). Close examination of the apical end of the CF revealed filamentous densities extending toward the PCR both in intact and detergent-extracted parasites, showing a close connection between the conoid and the PCR (Fig. 1*C*; *SI Appendix, Fig. S1 A–D*). These feature discoveries were enabled by the use of VPP imaging. We aligned and averaged 50 subvolumes of the region that includes the PCR pairing units, the anterior end of the CF, and the filamentous densities from six cellular tomograms. The averaged map shows that one CF spans about four ring-pairing units of the PCR (*SI Appendix, Fig. S1 E and F*). The filaments seen in Fig. 1*C* and *SI Appendix, Fig. S1 A–D* are not visible after averaging, probably because they are not always oriented in the same way. We annotated the reconstructed tomogram to directly examine the number of assembled CFs per apical complex, but the complexity and image limitations hindered our ability to trace them reliably. To reliably count the number of CFs in each conoid, we annotated the individual CF in detergent-extracted parasites, whose conoid is thin enough to be fully annotated; the results showed that each conoid consists of 14 ($n = 6$) or 15 ($n = 4$) CFs (*SI Appendix, Fig. S2 A–D*).

The SPMTs span most of the cell body length, contributing to the elongated shape of *Toxoplasma* tachyzoites because of their tight connection to the inner membrane complex (21). The SPMTs are defined as polar structures, emanating from the APR. Examination of the intact cell tomograms in the area of the APR revealed microtubules that are regularly and radially spaced around the ring, with additional discrete density appearing between neighboring SPMTs (white arrows in Fig. 1*D*). Annotation of the 3D volume allows us to count the number of SPMTs per cell that otherwise overlap or would be

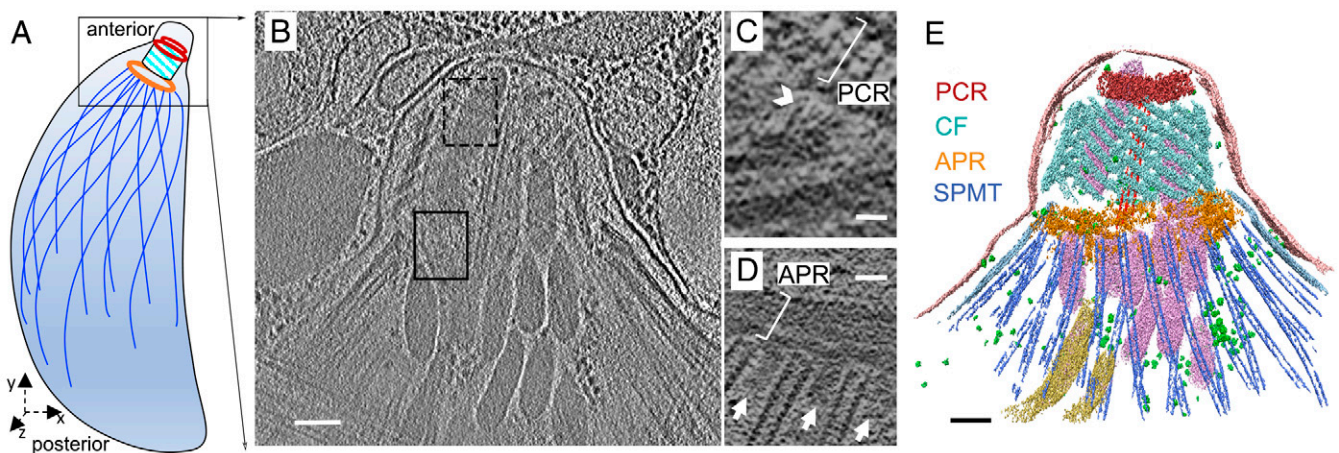


Fig. 1. Three-dimensional organization of the apical complex in *Toxoplasma* tachyzoites reveals the subpellicular microtubule and conoid architecture. (A) Cartoon of the *Toxoplasma* tachyzoite, the life stage of which has been imaged by cryo-ET in *B* and annotated in *E*. (B) Tomographic slice of a representative apical complex of an intact tachyzoite recorded with VPP optics in a 200-kV electron microscope. The dotted and solid rectangles show the regions of the apical complex represented in greater detail in *C* and *D* using different *z* slices (scale bar, 100 nm). (C) A zoomed-in view of a tomographic slice in the dashed black rectangle of *B*, showing two CFs in the *xy* plane, their anterior ends extending toward a PCR (white bracket) with filamentous density (a white arrowhead) between them (scale bar, 25 nm). (D) Portion of a tomographic slice in the black rectangle of *B*, showing the SPMTs in the *xy* plane, and their association with the APR (white bracket). Note columnar densities (white arrows) emerging from the APR and positioned between the SPMTs (scale bar, 25 nm). (E) Three-dimensional segmentation of the tomogram shown in *B* including the PCR (red), CFs (cyan), APRs (golden), SPMTs (blue), intraconoidal microtubules (red), micronemes (pink), rhoptries (yellow), and plasma membrane (pale pink) (scale bar, 100 nm). A movie with the complete tomogram is available in *SI Appendix, Movie S1*.

completely missed in a 2D slice view. To avoid potential uncertainty from intraconoidal or broken microtubules, we counted only the SPMTs emanating from the APR of intact parasites. The results showed that 15 of our tomograms displayed the previously reported number of 22 SPMTs, while 10, 6, and 1 tomograms showed 21, 23, and 24 SPMTs per cell, respectively (*SI Appendix, Fig. S2 E and F*).

SPMTs Contain Intraluminal Spirals (ISs) of Unknown Components, with Unique Organization at the Seam. Intact parasites are too thick to observe structures in most of the cell body at high resolution. To investigate the structural details of the SPMTs, therefore, detergent-extracted cells (*Materials and Methods*) were vitrified, imaged, and examined as done previously (5). The extracted cells are free of loosely bound cellular contents, thereby maximizing the signal/noise ratio of the remaining highly organized cytoskeleton components, especially the interior of the microtubules. The imaging magnification was chosen to optimally cover the microtubules as they emerge from the APR. The SPMTs of these lysed cells remain connected to the APR, together with interspersed pillar densities that were detected in the tomograms of intact parasites (Figs. 1*D* and 2*A*). These preserved details indicate that lysed cells have a similar cytoskeletal organization as intact cells. To obtain an intermediate resolution structure of these SPMTs, we performed subvolume alignment and averaged with 8-nm periodicity, based on the expected repeat for tubulin heterodimers and as also observed in the IS density repeats in Fig. 2*A* and previous reports (22). It has been shown previously that SPMTs have a standard microtubule arrangement (5, 23); our subvolume averaging assumed the tubulin protomers followed the microtubule-specific pseudohelical symmetry (24), in which

each microtubule consists of 13 protofilaments of alternating α - and β -tubulin, with a unique junction called the “seam,” where α - and β -tubulin interact laterally. This interaction is different from the other interactions between the protofilaments. Beginning and ending at the seam, there is a 12-nm axial spacing of a single spiral of α - or β -subunits. Our subvolume averaging resulted in a 6.7-Å resolution map for an SPMT segment over a length of 24 nm (Fig. 2*C* and *E*; *SI Appendix, Fig. S6C*). Visualizing the density, we were able to identify 5- to 7-Å-wide rod-shaped features, characteristic of α -helices, corroborating the subnanometer resolution estimate (Fig. 3*A–C*). The dispositions of these helices are consistent with the atomic structure of the tubulin molecules (25). However, the smoothness of the helix density suggests that the resolution appears to correspond to structural features expected in 7- to 8-Å-resolution cryogenic electron microscopy (cryo-EM) maps of single particles (26). Though our high-resolution results of individual monomers of tubulin or IS are derived from this map with the microtubule pseudohelical symmetry imposed, we also created a subtomogram average without imposing any symmetry (c1) using a search template having a well-defined seam, here called “symmetry-released” (*Materials and Methods*). While the symmetry-released map does not have sufficient resolution to distinguish α - and β -tubulin, the secondary structural elements of tubulin were apparent. Both maps were used for the interpretation of the topological organization of the SPMT and its associated IS.

In order to determine the relationship between the microtubule and the IS, we needed to distinguish between the α - and β -tubulin. It is known that *Toxoplasma*'s α - and β -tubulin are slightly different in their structure, with α -tubulin having a long S loop compared to β -tubulin, and that the sequences of both

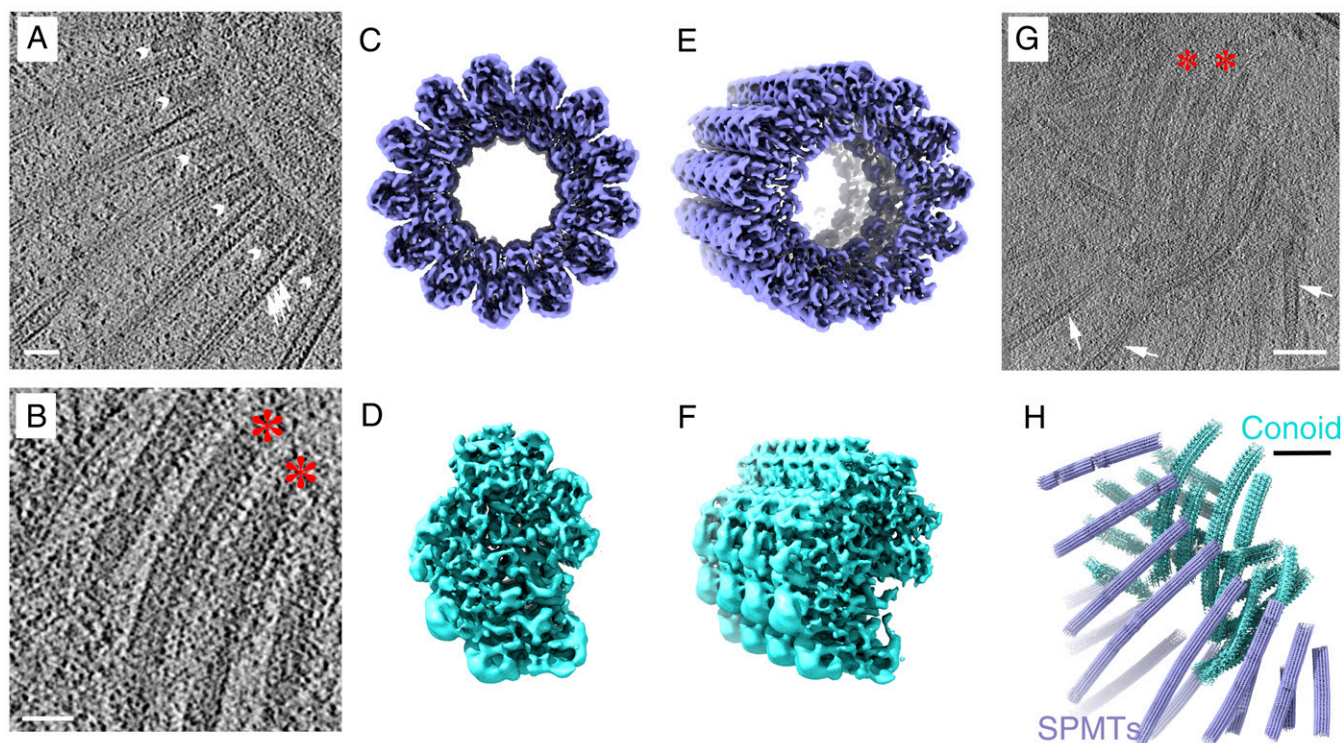


Fig. 2. Determination of the 3D structures of apical SPMT (blue) and CF (cyan) segments from detergent-extracted *Toxoplasma* with tilt series recorded in a 300-kV electron microscope. (A) Portion of a tomographic slice showing the SPMTs with internal striation density (white arrows) and short interspersed pillars (white arrowheads; scale bar, 50 nm). (B) Portion of a tomographic slice showing individual CFs (red stars; scale bar, 50 nm). (C, E) Reconstruction of a representative SPMT segment viewed from top and a tilted angle. (D, F) The top view and tilted view of a reconstructed CF segment showing an asymmetric semicircular profile. (G) A representative tomographic slice at the apical end of a detergent-extracted cell, containing individual SPMTs (white arrows) and CFs (red stars; scale bar, 100 nm). (H) The 3D organization of SPMTs and CFs in the local region of the reconstructed tomogram shown in G based on the refined coordinates of individual particles.

tubulins are ~85% identical to their mammalian counterparts (13). Based on that, we generated a homology model of *Toxoplasma* tubulins to distinguish the α - from the β -tubulin isoforms in the averaged density map. While the *Toxoplasma* genome carries three α -tubulin genes, we used the protein sequence of α -1 (TGME49_316400) for the homology model as it is the only one of the three that is appreciably expressed in tachyzoites, both at the RNA and protein level (14, 27), and, as therefore expected, it is also the only one of the three that appears essential for tachyzoite viability (28). The *Toxoplasma* genome also carries three β -tubulin genes (TGME49_266960, 221620, and 212240), with all isoforms reportedly detected in one proteomics study (14), although transcriptomic studies indicated the β -3 isoform (TGME49_212240) is essentially not expressed in tachyzoites (<https://toxodb.org/toxo/app>) and appears dispensable for tachyzoite growth (28); the other two genes are abundantly expressed in tachyzoites (<https://toxodb.org/toxo/app>) and appear essential (28). By amino acid sequence, β -1 (TGME49_266960) and β -2 (TGME49_221620) share 96.9% identity and 98.9% similarity; given this near complete identity, we chose the β -1 isotype at random for modeling purposes. The α -1 tubulin model displays the longer S loop compared to β -1, corresponding to residues 359 to 372 in the α -1 protein and similar to the resolved structure of the porcine microtubule. Our subtomogram average resulted in a map in which the α -tubulin is readily differentiated from the β -tubulin unit because of this difference in the S loop (Fig. 3 B and C). In summary, based on the correlation and visual analysis between the segmented tubulin subunit density in the subtomogram average and the map corresponding to ~8-Å resolution computed from the porcine α - and β -tubulin model (EMD-6439), we were able to distinguish these two subunits in our density map (Fig. 3A).

The IS is clearly visible in the cross-sectional view, lining the luminal surface of the microtubule protofilaments (Fig. 3D). Viewing from the longitudinal axis of the SPMT segment (Fig. 3E), this IS complex follows a left-handed and discontinuous helical pattern, built up stack by stack, similar to a series of split-ring washers (Fig. 3 E and F). The axial repeat of the washers is 8 nm along the microtubule axis, and the two split ends of each washer are about 12 nm apart (Fig. 3F), similar to the spirals of α - or β -tubulin. Based on the start and stop ends of each washer, we segmented 13 structurally similar repeating units X_1 to X_{13} in the symmetrized map, each estimated to be ~25 kDa based on the volume density (SI Appendix, Fig. S3) (29). In examining the density features of the IS units, each appears to have rod-shaped (α -helical) features, although the helices cannot be connected due to limited resolution (SI Appendix, Fig. S3D). Each IS stack is accompanied by a spiral of 13 rod-shaped densities (R_n) in green (SI Appendix, Fig. S3F), positioned between the IS components and the tubulin proteins and connecting between each spiral axially in the symmetrized average map (Fig. 3G; SI Appendix, Fig. S3F). Unwrapping the SPMT density map arbitrarily between protofilaments 4 and 5 further revealed the positioning of IS units with respect to the tubulin lattice, viewed from the luminal side (Fig. 3G). The organization of IS units and rod-shaped densities were also verified in symmetry-released maps (SI Appendix, Fig. S3F). However, the low visibility of unit X_1 in the symmetry-released map suggests that this unit located over the seam is not actually present but is an artifact of symmetry imposition (SI Appendix, Fig. S3F). Each putative monomeric unit of an IS spans between tubulin heterodimers in adjacent protofilaments and is positioned every 80 Å at the interface between an α -tubulin and the β -tubulin above it (SI Appendix, Fig. S4). The IS units marked X_2 to X_{13} are close to β -tubulin at residues 34 to 42, and the IS units marked R_2 to R_{13} are close to α -tubulin at two loops, residues 30 to 43 and 359 to 372 (the second is the S loop, which is longer in α - compared to β -tubulin).

SPMT Seams Are Oriented Nonrandomly with Respect to the Central Axis of the Parasites. Each IS is coaxial with the tubulin spirals, leaving a gap spanning a portion of the two protofilaments where the seam occurs. The unique arrangement of IS can also be observed in the averaged density map of SPMT segments computationally extracted from the intact (not detergent-extracted) parasites (Fig. 4A). This can be used to determine the orientation of the microtubule seam. We assigned the 3D SPMT averaged density map back to five reconstructed apical regions of intact parasite cells and retrieved the coordinates applied to align and average the subvolume particles. For each particle, we measured the microtubule seam orientation angle relative to the center of each cell body at cross-section (i.e., the z axis of each SPMT segment). For the five tomograms of intact parasites, half the segments, shown in Fig. 4C in pink, have a mode of their orientation of 10°, while the other half, shown in blue, have a mode in their orientations of 150° relative to the z axis (Fig. 4B). Overall, we find that the seam's orientation changes according to the position of the SPMT around the cell body and preferentially faces the center of the cell body (Fig. 4C). This nonuniform distribution of orientation is likely caused by specimen flattening during the freezing steps.

CFs Have an Unusual Tubulin-Based Structure with Additional, Unknown Densities Arranged Between the Protofilaments. Each CF is tightly associated with its neighbor filament, extending from the top PCR and forming an array of short left-handed spirals. Using detergent extraction to obtain relatively intact cytoskeletons, we were able to refine our subtomogram averaging of the CFs to reveal a periodic density of the CFs (Fig. 2B), which was identified to be 8- and 4-nm layer lines in Fourier space, similar to the typical microtubule tubulin repeats (5). Given previous work showing that tubulins are a main component of the CFs (5, 30), we sought to determine how the tubulins are assembled within these fibrils. To do this, we again used detergent-extracted tachyzoites to obtain their cytoskeleton as described for the SPMT experiments. This extraction preserves the overall helical shape of the CFs (Fig. 2 D–H) while allowing the cell body to be much thinner, improving the signal/noise ratio for tomographic images. The subtomogram averaged map of the CFs was determined at 9.3-Å resolution (SI Appendix, Fig. S6D). The density map accommodates nine columns or protofilaments of 40-Å repeated density that we are able to assign as a tubulin subunit using the homology model, together with uncharacterized associated density (Fig. 5). Although the data were not of sufficient resolution to visualize the difference between α - or β -tubulin, published proteomics analysis has shown that the CFs contain both (14). There are three lines of evidence that suggest the densities in the CF columns are tubulin. First is that the vertical repeat is consistent with that of tubulin dimers (80 Å). Second is that for several of the columns, the side-to-side spacing and angle are consistent with that of microtubules. Third, we have cross-correlated a Protein Data Bank (PDB) model of tubulin (PDB ID: 3jak) with the densities in the columns. The Z-score (31) varies from 2.5 to 14, which is higher than that of a random fit (SI Appendix, Fig. S5). We speculate that the differences in their shapes are due to differences in local resolution and conformational variability due to different interacting partners. The associated components in the center of the CF density map shapes the curvature of nine tubulin columns, with an opening between tubulin column 1 and 9. Three groups of densities are seen within the grooves between columns 3 and 4, 5 to 8, and 8 and 9 (Fig. 5 A and C), and these bind to alternating tubulin units every 80 Å axially (Fig. 5B). Compared to the density volume of tubulin monomer (55 kDa), the molecular weight of each repeating

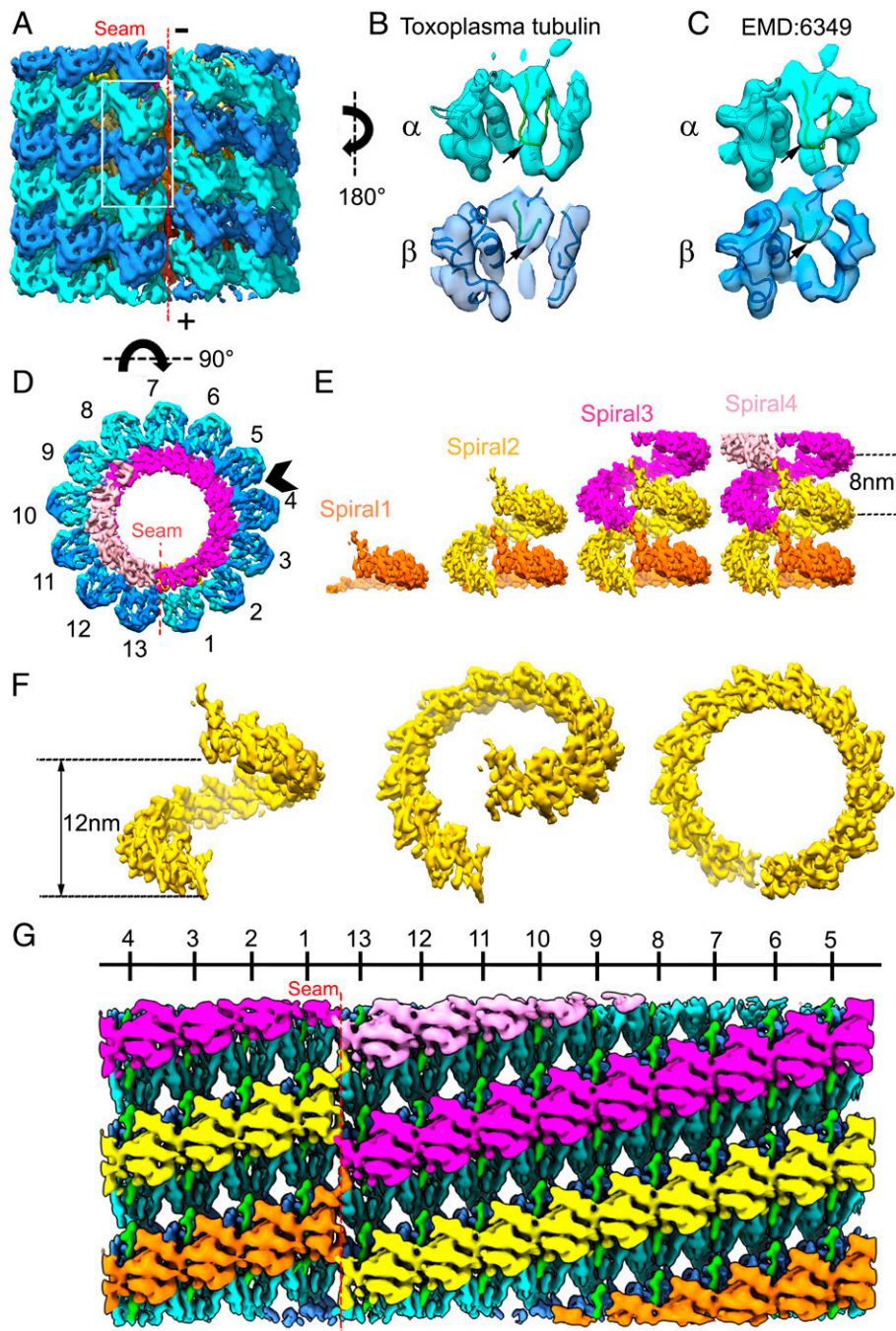


Fig. 3. Subtomogram average of SPMT tubulins and their associated lumen complex from detergent-extracted parasites. (A) The arrangement of α - (cyan) and β - (blue) tubulin subunits in the averaged density map of the SPMT segment, viewed from the seam and showing the arrangement of the 13 protofilaments. The plus (+) and minus (–) ends of the microtubule are as indicated. The minus (up) end is toward the APR. (B) Density for an $\alpha\beta$ -tubulin dimer as represented by the white boxed area of A, viewed from within the SPMT lumen. Note the S loop (green loop indicated by black arrows) in α -tubulin has extended density, but not in β -tubulin; this is validated by C, an $\alpha\beta$ -tubulin dimer segmented from a porcine microtubule (EMD6349) showing the S loop density of differences displayed at 8 Å, also viewed from the lumen side. (D) Nontubulin densities inside the tubulin spiral, viewed within a cross-section of SPMT, are colored. (E) Stacked spiral architecture of the IS complex with four stacked spirals shown in pink, magenta, yellow, and orange. (F) One stack of the IS in yellow viewed from the seam at different angles. (G) Unwrapping the SPMT between protofilaments 4 and 5, indicated by an arrowhead in D, shows the SPMT assembly from the inside, with an IS density axially arrayed along the tubulin lattice with apparent repeating units.

unit can be estimated to be about 30 kDa for each group between columns 3 and 4, 95 kDa for the ones between columns 5 and 8, and 20 kDa for the ones between columns 8 and 9.

The Plus End of CFs Is Oriented Toward the Top of the Conoid. With the successful composition assignment of tubulin in the

CFs, we were able to determine the structural polarity of the conoid. Fig. 5B shows that the plus ends of all nine protofilaments are directed toward the bottom of that figure, based on the fit of tubulin subunits modeled in the density map and by analogy to the plus end of canonical microtubules. This plus direction is toward the top (anterior end) of the conoid. This

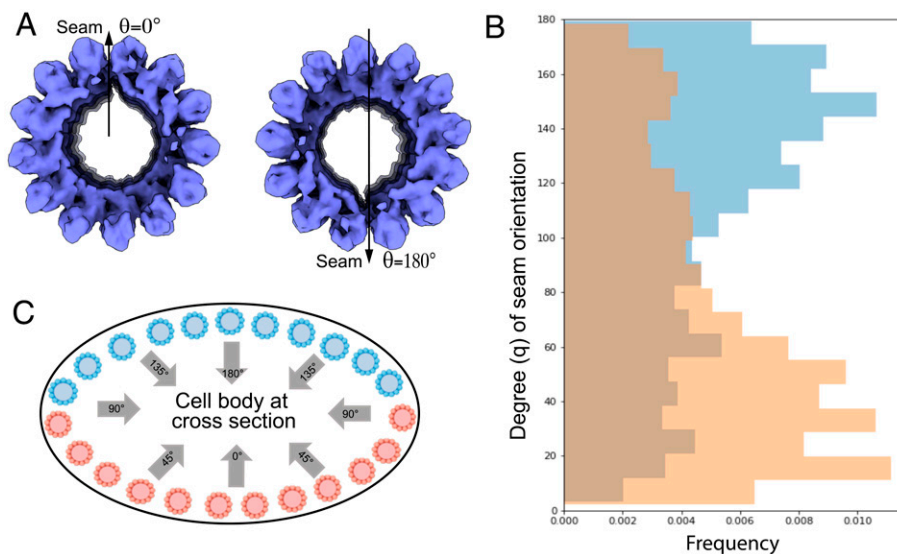


Fig. 4. The seam orientation of SPMT in tomograms of intact cells is nonrandom. (A) In-cell SPMT segment density is oriented with the seam facing down ($\theta = 180^\circ$) or up ($\theta = 0^\circ$). We used the gap in the cryo-EM density map of the SPMT segment as a marker of the microtubule seam. (B) The seam of apical microtubules along their axis is analyzed by measuring its angle relative to the z axis in cell tomograms ($n = 5$). (C) A schematic representation of SPMT models in the cell body at cross-section, based on the observed cross-section of the cell body in the tomograms. The blue color is used for the microtubules in the “top” half layer of the cell (i.e., toward the electron beam), and the orange color is used for the microtubules in the “bottom” half of the cell. Note that the seam is predominantly oriented toward the center of the somewhat flattened cell body, with orientation angle $90^\circ < \theta < 180^\circ$ for SPMTs in blue or $0^\circ < \theta < 90^\circ$ for SPMTs in orange.

polarity direction suggests that the conoid is assembled from its base toward what will ultimately be its anterior end. Within the density of extracted CF segments, the nine tubulin columns are organized into a comma shape in cross-section (Fig. 6A). The interprotofilament angles of CFs are much more variable and often much greater than the relatively constant $\sim 27^\circ$ of the interprotofilaments in SPMTs (Fig. 6E–G). Interestingly, there is a very pronounced kink between protofilaments 3 and 4, possibly as a result of the observed density between these two protofilaments (magenta in Fig. 6).

Extensive density can be resolved within the structure of the CF segments averaged from intact cells, but to a lower resolution than described above for the detergent-extracted parasites. Nevertheless, we were able to readily fit the higher-resolution CF structure into the structure obtained from intact cells with protruded conoids. The results showed considerable extra density within the CFs of intact cells, arrayed along the outside of the tubulin-based protofilaments and associated densities seen for the detergent-extracted parasites (Fig. 6B). Presumably, this extra material dissociates upon detergent extraction. To determine the polarity orientation of the CFs within the cell, their in situ density was mapped back to the cell tomogram based on the coordinates of each extracted particle. The CF segment density revealed the orientation of the CFs to be in “parallel” with respect to each other, with the opening of the cross-sectional comma shape being toward the center of the conoid (Fig. 6C and D). The patterning of retracted and protruded conoids in calcium ionophore-stimulated parasites was further investigated by measuring the spacing of neighboring fibrils and the ratio between turn and rise distance along the axis under these two conditions (Fig. 6I and J). The results indicated that relative to retracted conoids, the distance between neighboring fibrils is slightly increased when the conoid is protruded, with a median spacing of 38.4 nm in the protruded conoid versus 32.6 nm in the retracted structures. In addition, the turn/rise ratio was markedly lower in the protruded versus retracted conoids (medians of 1.48 and 2.55, respectively).

Discussion

Single-particle cryo-EM of thin or purified samples is ideal to determine near atomic resolution structures of biomolecules in solution; however, this usually comes at the expense of studying the cellular context of their native environment. Here, we developed a protocol for image acquisition and processing by cryo-ET to investigate the cytoskeleton-based apical regions of *Toxoplasma*, examining the cellular machinery in context both in intact and detergent-extracted parasites and extending to the level of single macromolecules in detergent-extracted parasites at subnanometer resolution. Cryo-ET of intact parasites revealed the spatial organization of distinct components in the highly crowded apical region. By annotating the tubulin-based SPMTs and CFs, we conclude that their numbers are not fixed, implying that their assembly process is regulated but not rigid (SI Appendix, Fig. S2D and F). Interestingly, lower expression rates of α -tubulin in *Plasmodium berghei* resulted in fewer microtubules (32). Further investigation into the relationship between SPMT and CF numbers and tubulin expression in *Toxoplasma* will be interesting to study.

The SPMT minus end emanates from the APR, which has been suggested to function like a microtubule organizing center, i.e., as an anchoring site for the SPMTs (23). Previous studies revealed that even in the absence of fully formed APR, there remains some organization of the SPMT array (33). This argued for additional elements that support and stabilize the arrangement of the SPMT. The pillar densities we observe between neighboring SPMTs (Figs. 1D and 24) where they attach to the APR could be involved in such organization. The identities of these short densities are not yet known, but they may be related to previously described structure found between the SPMTs (23) and could possibly be composed of the recently discovered AC9 and/or AC10 proteins, which by light microscopy are found just below the APR (34, 35).

How the APR associates with the conoid in parasites with a protruded conoid and whether there is a direct physical connection between the two after conoid protrusion remain to be determined. RNG2 has been observed to occupy a position

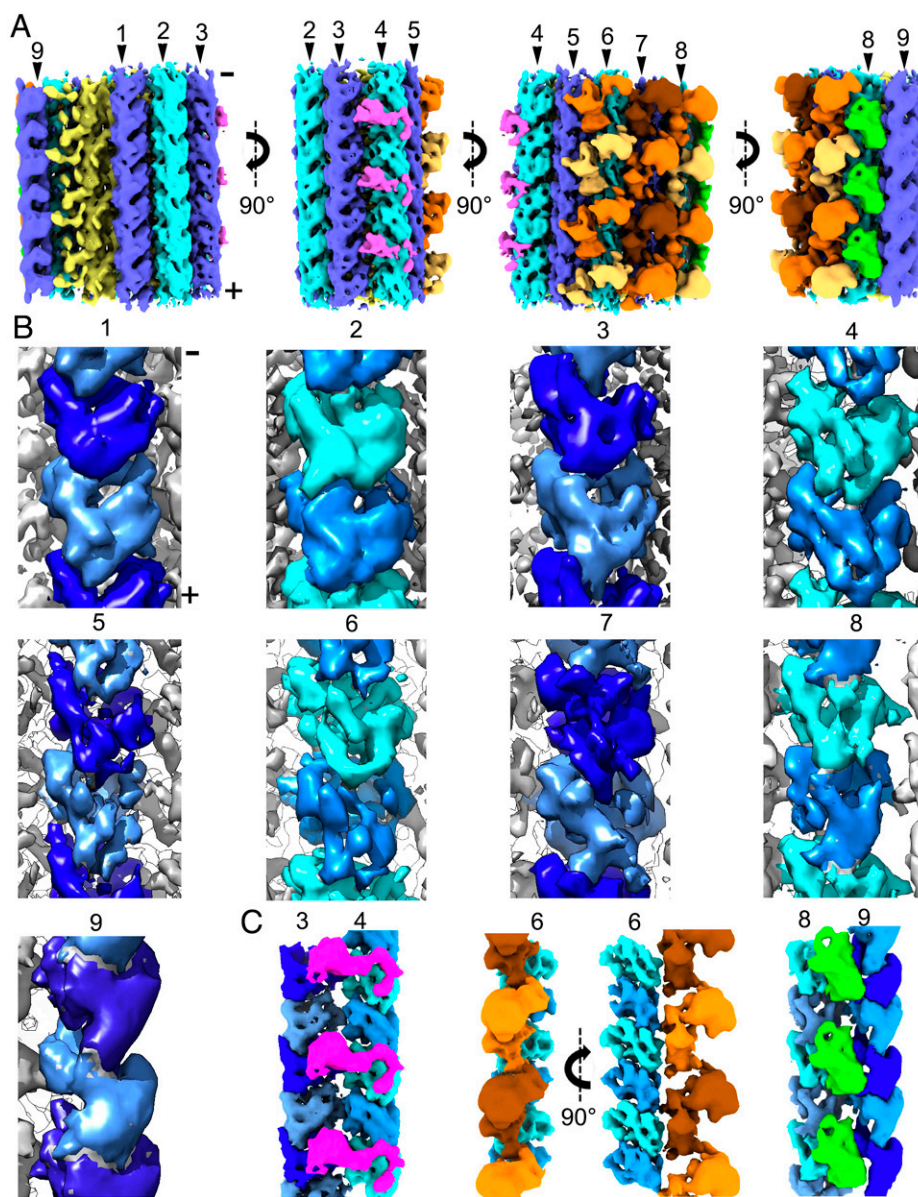


Fig. 5. Variable resolvability of tubulin in a CF segment of cryo-EM density by subtomogram averaging from detergent-extracted parasite. (A) CFs are unusual tubulin-based fibrils. Each fibril contains nine columns of tubulin (blue and cyan), associated with CF-associated densities within the concave inner face of the CF (yellow) and on the outer convex face (magenta, green, orange). This is shown axially from various views rotated around the long axis. (B) Zoomed-in cryo-EM density of two tubulin components in each of columns 1 to 9. Tubulin columns were fitted to the conoid average densities. A total of nine columns were segmented, shown axially with alternating light and dark blue colors (top) from various views. (C) Nontubulin groove densities appear every 80 Å, shown between columns 3 and 4 (magenta), on the outside of columns 5 to 8 (orange and brown), and between columns 8 and 9 (green). The plus (+) and minus (−) ends of the microtubule are as indicated in A and the first column of B.

consistent with such a role and so could serve to link the two (36). In the analyses described here, we did not see any direct connection between these two key structures. There is no evidence to suggest how such a large structure as the conoid can be reversibly protruded if it were physically linked to the APR. On the other hand, we did see intimate connections in the form of discrete filaments connecting the PCR and the anterior ends of the CFs. Enabled by the VPP and subtomogram averaging, we also determined a ratio of four PCR subunits for every CF (*SI Appendix, Fig. S1 E and F*); whether this number differs for conoids with 14 versus 15 CFs is not yet known and, if it does, whether the number of the PCR subunits determines the number of the CFs (or vice versa) remain to be determined.

Using detergent-extracted parasites and advanced subtomogram averaging protocols for filament structures allowed us to

resolve α - and β - tubulin within the SPMTs at subnanometer resolution, as well as observing an inner spiral of ordered density lining the SPMT lumen as was previously reported but not studied in detail (22, 37). Microtubule assembly by α -tubulin and β -tubulin usually forms a hollow tube, but the formation of microtubules with lumen spirals has been observed in human sperm tails and implicated in flagellar rigidity and directional migration (37). The presence of ISs and the nonrandom orientation of the seam likely play as yet undetermined but critical roles in *Toxoplasma* biology. The SPMTs are reported to be unusually stable in the cold upon ionic detergent treatment (5, 38), and their ends are presumably uncapped as seen in sporozoites of the related apicomplexan parasites, *Eimeria* and *Plasmodium* (22, 39), conditions that can normally cause microtubule disassembly (40, 41). Assuming the IS complex extends

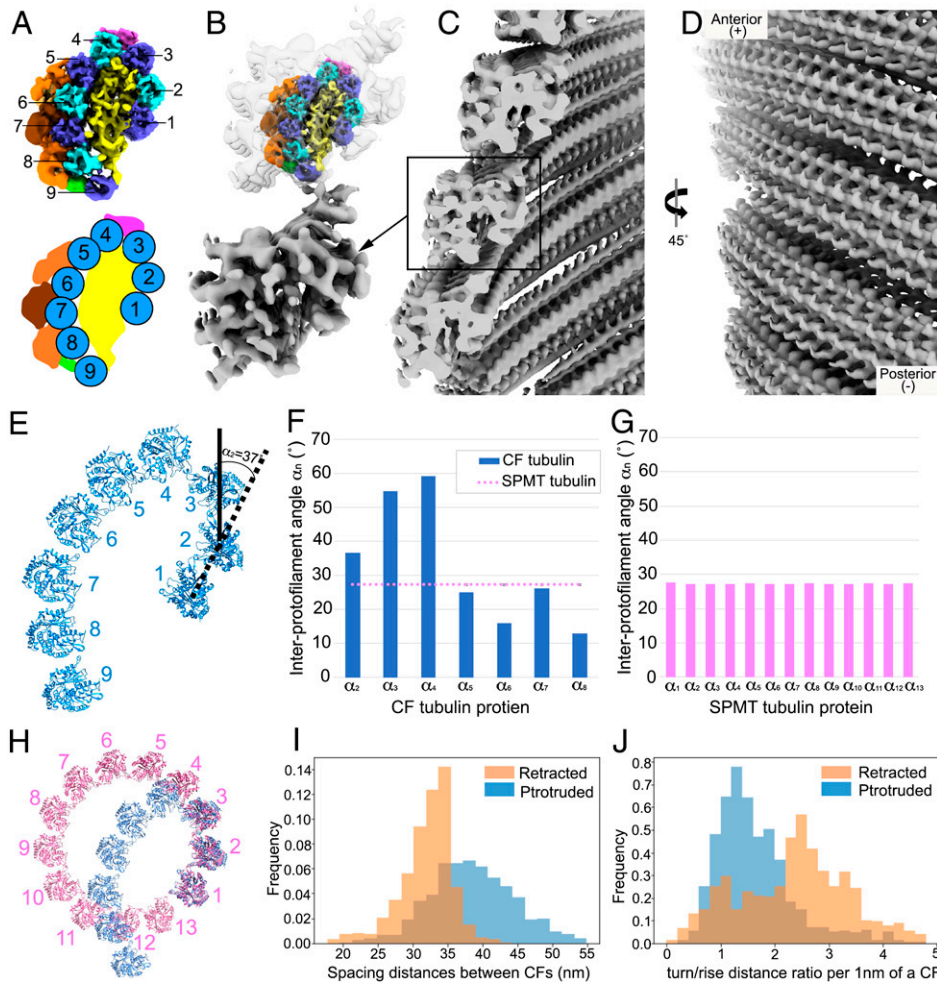


Fig. 6. CFs are oriented in parallel with a plus-like end at the anterior. (A) Reconstruction of a CF segment from protruded conoids from detergent-extracted cells, generated by subtomogram averaging and shown in cross-section, viewed from the minus-like end. The cartoon (on the *Bottom*) illustrates the structural arrangement of the nine tubulin columns that form the comma-like architecture. (B) Low-resolution reconstruction of a CF segment from conoid-protruded intact cells, generated by subtomogram averaging. Above this is shown the higher-resolution structure of A inserted into the low-resolution structure from intact cells. (C) The CFs in a protruded conoid are assembled into spiral filaments with a “parallel” orientation and the opening of the comma shape facing the interior of the conoid. (D) The spiral CFs viewed from the conoid surface. (E) Zoomed-in model of tubulins within a CF segment. An example of how interprotofilament angles were determined is shown for the angle between a line connecting the centers of protofilaments 1 and 2 relative to such a line for protofilaments 2 and 3; this was defined as α_2 and was determined to be 37° . (F) The interprotofilament angles were measured for each protofilament relative to the ones on either side. (G) As for F, except the interprotofilament angles were measured for the SPMT protofilaments. (H) Comparison of the protofilament arrangement in the SPMTs and CFs with the tubulin model fitted into the cryo-ET density map. Note the marked kink at protofilaments 3 and 4 in the CF. (I) Closest spacing distance between neighboring CFs showing the increased spacing in protruded CFs (blue) relative to retracted ones (orange). Data are from analysis of three protruded and four retracted conoids of intact cells. (J) The turn/rise distance ratio was measured every 1 nm along the CF axis, showing that the CFs in retracted (orange) conoids are higher than in protruded conoids (blue).

the length of the SPMT, it might serve to stabilize the SPMTs, preventing dynamic turnover from constantly occurring at the plus end. They might also indirectly affect the external surface of the tubulin lattice by inducing some curvature of the microtubule. Indeed, the pellicle formed by the SPMTs has a small but distinct helical pitch that correlates with the axis of attachment to solid substrates and the resulting path taken during gliding motility (21, 42, 43). Whether this is inherent to the SPMTs or is an organization mandated by other cellular components such as the alveolar membranes is not yet known, but helical reinforcement is an efficient solution regularly used in engineering to provide strength, e.g., in carbon-fiber tubes or in armored hoses. The molecular constituents of the IS should be among the proteins detected in proteomic studies of purified parasite cytoskeletons (14, 27, 44). The structural information gleaned here was not of sufficient resolution to allow predictions about such identities to be made, but higher resolutions

might; alternatively, structural determination of individual purified proteins would likely enable assignment of the densities to individual molecules in the same way we did here with the well-characterized α - and β -tubulins. Potential mechanisms for controlling the orientation of the SPMT seam, which is specified by the lumen spirals and observed here to have a predictable orientation relative to the cell’s long axis, should be further characterized to understand the role of the seam during motility and invasion.

While this manuscript was under review, a single-particle cryo-EM analysis of the SPMTs was reported by Sibley, Zhang, and colleagues resolving the tubulins and IS subunits at near atomic resolution (45). In comparing their structures and our subtomogram averages with or without microtubule symmetry imposition, the assembly organization and internal subunit structure of tubulin agree very well. They identified the main components of the IS as TrxL1, TrxL2, and SPM1 (*SI Appendix, Fig. S7*). These

identifications were corroborated by deleting the relevant genes and showing the SPMTs' stability and integrity upon chemical challenge were compromised. In our subtomogram average maps, the identified α -helices in the IS subunit match well with those in the TrxL1 model (*SI Appendix, Fig. S3*). We recognized that a symmetrized subtomogram average map could bias the topological relationships among the IS subunits, but it will have higher resolution for the subunits, which are in fact related by that symmetry. Therefore, we compared our symmetry-released map with the single-particle map for the overall organization of ISs in SPMT. It is apparent that 10 of the IS subunits (X_2 to X_{13} , except for X_2 and X_8) agree well with the single-particle map in terms of their density feature and spatial distribution. The PDB model for TrxL1 (45) was also fitted well to our segmented densities for IS units (*SI Appendix, Fig. S7E*). This corroboration strongly indicates that our independent approaches validate each other in terms of their reliability. However, we do not see a substantial structural difference between X_2 , X_8 , and the other 10 subunits (X_3 to X_7 , X_9 to X_{13}) in our symmetry-released map. The basis for this difference is not known but could be due to the fact that different zones of the cell body were imaged and analyzed in these two studies (the apical end of the SPMT in our case and the mid- and posterior regions in their study) (46, 47). In any case, the density around the seam is missing in both our symmetry-released structure and their single-particle structure.

We were also able to generate a molecular model for the CF tubulin based on the subnanometer cryo-EM density map. By fitting the tubulin subunit model to the density map of the nine protofilaments comprising a CF, we affirmed that the comma-shaped geometry of the CF is an unusual mode of tubulin polymerization unique to the Apicomplexa. We determined that the assembly of tubulins in the conoid incorporates different tubulin monomers based on the fitting cross-correlation, but we were unable to distinguish between α -tubulin and β -tubulin, as we were able to do for the SPMTs, nor were we able to determine which isoforms of these two proteins were present. The orientation of the tubulin subunits in the CF suggests that it is assembled with a plus end facing the anterior end of the conoid. The densities observed decorating the interior and exterior parts of the tubulin-based portions of the CFs might play a role in the modification of CF curvature. The largest angle ($\sim 60^\circ$) between protofilaments 3 and 4 seems likely to be related to the groove density uniquely observed in this location (magenta in Fig. 6B). Although the identity of the protein(s) represented by this density has not yet been determined, recent studies have shown that *Toxoplasma gondii* doublecortin-domain protein (TgDCX) exclusively localizes to the conoid, where it helps stabilize and retain the curvature of the CFs (7, 48), and the size of TgDCX is consistent with the observed density. Also consistent with this possibility, cryo-EM density of conventional microtubules polymerized with bovine brain tubulin in vitro shows that the 80-Å periodicity of human doublecortin (DCX) is patterned axially between the tubulin protofilaments and that DCX is necessary for the observed curvature of the protofilaments relative to one another in cross-section of microtubules in vitro (49, 50). TgDCX also induces the curved microtubule arcs in *Xenopus* S3 cells (7).

Conoid protrusion has been suggested to involve modifications in CF patterning (5, 7). The relative angle of each CF to the base of the conoid was revealed to be increased in protruded conoids compared to retracted ones, and our data support this observation with a lower turn/rise distance ratio in protruded conoids (Fig. 6J), suggesting that protruded CFs are less twisted than retracted CFs. We also observed a wider spacing between CFs in the protruded conoid, and it is possible that this is related to the changes in the turn/rise along the fibril length. The progressively decreased resolvability from tubulin protofilaments 1 through 9 in the subtomogram averaging

suggests that the "gap" in the comma-shaped cross-section of CFs is flexible, perhaps causing the fibril to twist, hence the spacing changes shown in Fig. 6I.

Tachyzoites utilize tubulins for different macromolecular assemblies in a novel way. In this study, we substantially refined two molecular structures of the tubulin-based elements in the apical region, SPMTs and CFs, revealing two very different forms of structural arrangements (*SI Appendix, Movie S2*). This work and its relation to cellular context, therefore, provide structural detail for the two most substantial forms of tubulin assemblies at the apical end of *Toxoplasma* parasites, the portion of this intracellular parasite that is crucial to the process of host cell invasion. It also provides deeper understanding of diverse assemblies of macromolecular complexes in the same cell and in those molecules' native environment.

Materials and Methods

Parasite Maintenance and Cell Culture. *T. gondii* RH Δ hxgprt strain was maintained by growth in confluent primary human foreskin fibroblasts (HFFs) in Dulbecco's modified Eagle's medium (Invitrogen) with 10% fetal bovine serum (HyClone), 2 mM glutamine, 100 U/mL penicillin, and 100 μ g/mL streptomycin at 37°C in 5% CO₂. The HFFs are fully deidentified and therefore do not constitute human subject research.

Parasite Preparation for Cryo-EM. Parasites were released from heavily infected monolayers of HFFs by mechanical disruption of the monolayers using disposable scrapers and passage through a 25-gauge syringe. The parasites were added to fresh monolayers of HFFs and 18 to 20 hpi, were washed two times with Hank's balanced salt solution (HBSS without calcium, magnesium, and phenol red; Corning) supplemented with 1 mM magnesium chloride, 1 mM calcium chloride, 10 mM sodium hydrogen carbonate, and 20 mM Hepes (pH 7). HFFs were scraped into fresh HBSS, and tachyzoites were mechanically released and treated with calcium ionophore (A23187; Sigma-Aldrich) at a final concentration of 1 μ M for 10 min at room temperature. Tachyzoites were pelleted and resuspended in fresh HBSS.

To make detergent-extracted tachyzoites, after incubation with calcium ionophore, parasites were pelleted and gently resuspended in 10 mM sodium deoxycholate in phosphate buffered saline (PBS), supplemented with protease inhibitor (cOmplete; Sigma-Aldrich). After incubation of 10 min at room temperature, tachyzoites were pelleted and immediately loaded on EM grids or resuspended in PBS and pelleted again before loading.

Cryo-ET. Plasma-treated lacey carbon EM grids were mounted on a manual plunger, loaded with intact or detergent-treated parasite suspension mixed with 10- or 6-nm gold fiducials (EMS), blotted from the back side using Whatman paper #5, and plunged into liquid ethane at near-liquid nitrogen temperature.

Detergent-treated tachyzoites were imaged using a Titan Krios electron microscope (Thermo Fisher Scientific) equipped with a field emission gun operated at 300 kV, an energy filter (Gatan) operated at zero loss, and a K2 Summit direct electron detector (Gatan). High-magnification images of SPMTs and CFs were recorded at 105,000 \times and 81,000 \times , respectively, corresponding to a pixel size of 1.38 and 1.77 Å. Tilt series were recorded using Tomo4 software with bidirectional acquisition schemes (51), each from -45° to 45° with 3° increment. The target defocus was set to -1.0 to -4.0 μ m. The K2 camera was operated in dose fractionation mode recording frames every 0.15 or 0.2 s. The total dose was limited to 90 to 100 e/Å² for conoid datasets and 120 to 140 e/Å² for SPMT datasets.

The tachyzoites in fresh HBSS were imaged using a Talos Arctica electron microscope (Thermo Fisher Scientific) equipped with a field emission gun operated at 200 kV, a VPP (20), an energy filter (Gatan) operated at zero loss, and a K2 Summit direct electron detector (Gatan). Upon phase plate alignment and conditioning, tilt series of intact parasites were recorded at 39,000 \times at pixel size 3.54 Å using Tomo4 software with bidirectional acquisition schemes, each from -60° to 60° with 2° or 3° increment. The target defocus was set to -1.0 μ m. The K2 camera was operated in dose fractionation mode recording frames every 0.6 s. Every two or three tilt series, a new spot on the phase plate was selected. The phase shift spans a range from 0.2 to 0.8π . The total dose was limited to 70 to 90 e/Å².

Tomography Reconstruction and Analysis. The movie frames were motion corrected using motionCor2 (52), and the resulting micrographs are compiled into tilt series. Tilt series alignment, tomogram reconstruction, and contrast transfer function estimation are performed automatically using the

tomography pipeline in EMAN2 (16), except the reconstructed tomogram in Fig. 1, which was performed by IMOD (53, 54). Subcellular features were semi-automatically segmented using the EMAN2 convolutional neural network (15) and refined manually using Chimera (55).

For SPMTs (see flowchart, *SI Appendix, Fig. S6A*), the SPMTs from the intact parasite dataset are selected by manual tracing, and subtomograms are generated along the trace. A total of 1,994 particles from 10 tomograms are included in the averaged structure of microtubules from the cellular tomograms. The microtubule pseudohelical symmetry (25) is applied during the refinement. For SPMTs from the detergent-treated dataset, particles are selected automatically using the neural network-based particle picker in EMAN2 (16). De novo initial models are directly generated from the particles. The averaged structure of the SPMT is produced from 39,122 particles from 90 tomograms of detergent-extracted parasites using the subtomogram and subtilt refinement pipeline in EMAN2. The microtubule pseudohelical symmetry (25) is applied during the refinement, as well as a final symmetry-released map without this symmetry applied to the average.

For CFs (see flowchart, *SI Appendix, Fig. S6B*), the CFs from both non-detergent-treated and detergent-treated datasets are selected manually using the filament tracing tool in EMAN2 (16). Subtomograms are then generated along the trace with a 75% overlap between neighboring particles. De novo initial models are directly generated from the particles. For the in situ CF structure, 1,940 particles from six tomograms are used in the subtomogram average. For the CFs from detergent-treated cells, 29,524 particles are generated from 126 tomograms.

For both CFs and SPMTs, subsequent local refinements are performed by extracting subparticles based on the original subtomogram refinement focusing on different regions of the averaged structure. Further analysis of tubulin-based features, including the orientation of the seam line of microtubules, spacing, and curl distribution of the conoid, are computed based on the particle position and orientation from the corresponding subtomogram refinement. Tools for these analyses are distributed within the latest EMAN2 package.

Map Segmentation and Modeling. The SPMT map from detergent-treated cells was segmented with Segger (version 2.5.4) in Chimera (version 1.13), with grouping by smoothing, four steps of size 1; this generated ~260 regions. Groups of two regions appeared to resemble the V-like shape of individual tubulin protein. Chains representing α - and β -tubulin subunits were respectively fitted to groups of two regions (with the V shape) with the SegFit tool in Segger (29). The fits with the top score matched the map well, with secondary structures in the map and model agreeing well; Z-scores were ~20 (31), indicating high confidence that the fit is correct. The α - and β -subunits were distinguished in the map based on the S loop, which is longer in α - (residues 359 to 372) than in β - (residues 358 to 362) subunits. ISOLDE in ChimeraX was then used to refine the models better into the map (56). The modified models for α - and β -subunits were fitted to each column, creating 13 columns of 6 proteins per column to completely cover the tubulin part of the map.

A map of the symmetrized IS was generated by subtracting densities corresponding to α - and β -tubulin from the entire symmetrized SPMT map. This IS map was then segmented with Segger without any grouping steps. Rod-shaped regions were grouped interactively, and a cylinder representing an

α -helix was fitted to each. A β -sheet with three strands was fitted to a flat region in the middle. The helices and strands were joined such that a combined pseudo-model consisting of 16 helices and 3 β -strands could be replicated 13 times per spiral, accounting for most observed densities. These units were named X_1 to X_{13} . Between the IS and the tubulin protein subunits, 13 further rod-shaped fragments were also observed, and a pseudo-model was built for these separately and marked R_1 to R_{13} . The helical and β -sheet pseudo-models were built with custom scripts in Chimera. A symmetry-released IS map was generated by subtracting densities of α - and β -tubulins from the entire symmetry-released map. This map was then segmented with Segger with no grouping steps, and regions were grouped based on which pseudo-model of the X or R unit they overlapped the most.

Tubulin proteins from SPMT were fitted into the cryo-EM density maps of CFs from detergent-extracted cells by exhaustive search with Situs (57). Top-scoring fits placed tubulin proteins in columns, much like in the SPMT. Nine columns were found, following a curved open path, with ~8/9 tubulin proteins per column. The fitted proteins were used to mask the CF map (zone tool, 4-Å radius) to form the conoid tubulin map. The conoid tubulin map was segmented using the fitted models (using Segger, SegFit, and the Group Regions by Chains function). Fitting individual tubulin proteins to each region with SegFit rotational search reproduced the fits, with Z-scores of ~4. Secondary structures in the form of rods are marginally visible in the map, and these corresponded to helices in the fitted models. Extracted tubulin densities from each column were fitted to a single region in the same column using SegFit to study whether there is a repeating α - or β -like pattern. The conoid tubulin map was further subtracted from the CF map to form the nontubulin map. Some repeating densities with clear boundaries could be seen and were extracted with Segger.

Data Availability. The tomograms of intact and detergent-extracted *Toxoplasma* apical end and subvolume averages of SPMTs and CFs are deposited to EMDDataBbank database (www.emdatabank.org) with the accession code [EMD-26019](#) for the symmetrized SPMT map, [EMD-26018](#) for the symmetry-released SPMT map, and [EMD-26020](#) for the CF map from detergent-extracted cells; [D_1000260658](#) for the SPMT map, [EMD-26009](#) for the CF map, and [EMD-26008](#) for the CF anterior end and PCR units from intact cells; and [EMD-26007](#) for the tomogram of intact *Toxoplasma* apical end and [EMD-26006](#) for the tomogram of detergent-extracted parasitic cells. The atomic coordinates have been deposited in the Protein Data Bank (www.pdb.org), with PDB accession codes [7TNS](#), [7TNQ](#), and [7TNT](#). All study data are included in the article and/or supporting information.

ACKNOWLEDGMENTS. We thank Dr. Ke Hu and Dr. John M. Murray from Arizona State University for helpful discussion during this work. We thank Dr. Rui Zhang from Washington University for helpful discussion during the manuscript revision. We thank the Chan Zuckerberg Biohub Inter-campus Team Award for supporting this research. Other support includes NIH Grants (S10OD021600, P41GM103832, R01GM079429, P01GM121203, and R21MH125285-01A1), the United States-Israel Binational Agricultural Research and Development Fund, Vaadia-BARD Postdoctoral Fellowship Award no. FI-582-2018, the Stanford Maternal and Child Health Research Institute, and Stanford School of Medicine Dean's Postdoctoral Fellowship.

1. J. P. Dubey, *Toxoplasmosis—A waterborne zoonosis. Vet. Parasitol.* **126**, 57–72 (2004).
2. V. Carruthers, J. C. Boothroyd, Pulling together: An integrated model of *Toxoplasma* cell invasion. *Curr. Opin. Microbiol.* **10**, 83–89 (2007).
3. D. J. Dubois, D. Soldati-Favre, Biogenesis and secretion of micronemes in *Toxoplasma gondii*. *Cell. Microbiol.* **21**, e13018 (2019).
4. R. Ben Chaabene, G. Lentini, D. Soldati-Favre, Biogenesis and discharge of the rhoptries: Key organelles for entry and hijack of host cells by the Apicomplexa. *Mol. Microbiol.* **115**, 453–465 (2020).
5. K. Hu, D. S. Roos, J. M. Murray, A novel polymer of tubulin forms the conoid of *Toxoplasma gondii*. *J. Cell Biol.* **156**, 1039–1050 (2002).
6. A. Graindorge *et al.*, The conoid associated motor MyoH is indispensable for *Toxoplasma gondii* entry and exit from host cells. *PLoS Pathog.* **12**, e1005388 (2016).
7. J. M. Leung *et al.*, A doublecortin-domain protein of *Toxoplasma* and its orthologues bind to and modify the structure and organization of tubulin polymers. *BMC Mol. Cell Biol.* **21**, 8 (2020).
8. E. Lycke, K. Carlberg, R. Norrby, Interactions between *Toxoplasma gondii* and its host cells: Function of the penetration-enhancing factor of *Toxoplasma*. *Infect. Immun.* **11**, 853–861 (1975).
9. N. Morrisette, M.-J. Gubbels, “The *Toxoplasma* cytoskeleton: Structures, proteins, and processes” in *Toxoplasma gondii*, L. M. Weiss, K. Kim, Eds. (Academic Press, ed. 3, 2020), pp. 743–788.
10. N. Dos Santos Pacheco, N. Tosetti, L. Koreny, R. F. Waller, D. Soldati-Favre, Evolution, composition, assembly, and function of the conoid in Apicomplexa. *Trends Parasitol.* **36**, 688–704 (2020).
11. T. J. Stokkermans *et al.*, Inhibition of *Toxoplasma gondii* replication by dinitroaniline herbicides. *Exp. Parasitol.* **84**, 355–370 (1996).
12. N. S. Morrisette, A. Mitra, D. Sept, L. D. Sibley, Dinitroanilines bind alpha-tubulin to disrupt microtubules. *Mol. Biol. Cell* **15**, 1960–1968 (2004).
13. S. D. Nagel, J. C. Boothroyd, The alpha- and beta-tubulins of *Toxoplasma gondii* are encoded by single copy genes containing multiple introns. *Mol. Biochem. Parasitol.* **29**, 261–273 (1988).
14. K. Hu *et al.*, Cytoskeletal components of an invasion machine—The apical complex of *Toxoplasma gondii*. *PLoS Pathog.* **2**, e13 (2006).
15. M. Chen *et al.*, Convolutional neural networks for automated annotation of cellular cryo-electron tomograms. *Nat. Methods* **14**, 983–985 (2017).
16. M. Chen *et al.*, A complete data processing workflow for cryo-ET and subtomogram averaging. *Nat. Methods* **16**, 1161–1168 (2019).
17. C. V. Robinson, A. Sali, W. Baumeister, The molecular sociology of the cell. *Nature* **450**, 973–982 (2007).
18. D. Tegunov, L. Xue, C. Dienemann, P. Cramer, J. Mahamid, Multi-particle cryo-EM refinement with M visualizes ribosome-antibiotic complex at 3.5 Å in cells. *Nat. Methods* **18**, 186–193 (2021).
19. R. Mondragon, E. Frixione, Ca(2+)-dependence of conoid extrusion in *Toxoplasma gondii* tachyzoites. *J. Eukaryot. Microbiol.* **43**, 120–127 (1996).
20. R. Danev, B. Buijsse, M. Khoshouei, J. M. Plitzko, W. Baumeister, Volta potential phase plate for in-focus phase contrast transmission electron microscopy. *Proc. Natl. Acad. Sci. U.S.A.* **111**, 15635–15640 (2014).

21. N. S. Morrisette, J. M. Murray, D. S. Roos, Subpellicular microtubules associate with an intramembranous particle lattice in the protozoan parasite *Toxoplasma gondii*. *J. Cell Sci.* **110**, 35–42 (1997).
22. M. Cyrklaff *et al.*, Cryoelectron tomography reveals periodic material at the inner side of subpellicular microtubules in apicomplexan parasites. *J. Exp. Med.* **204**, 1281–1287 (2007).
23. B. A. Nichols, M. L. Chiappino, Cytoskeleton of *Toxoplasma gondii*. *J. Protozool.* **34**, 217–226 (1987).
24. H. Sui, K. H. Downing, Structural basis of interprotofilament interaction and lateral deformation of microtubules. *Structure* **18**, 1022–1031 (2010).
25. R. Zhang, E. Nogales, A new protocol to accurately determine microtubule lattice seam location. *J. Struct. Biol.* **192**, 245–254 (2015).
26. W. Chiu, M. L. Baker, W. Jiang, M. Dougherty, M. F. Schmid, Electron cryomicroscopy of biological machines at subnanometer resolution. *Structure* **13**, 363–372 (2005).
27. C. T. Gómez de León *et al.*, Proteomic characterization of the subpellicular cytoskeleton of *Toxoplasma gondii* tachyzoites. *J. Proteomics* **111**, 86–99 (2014).
28. S. M. Sidik *et al.*, A genome-wide CRISPR screen in *Toxoplasma* identifies essential Apicomplexan genes. *Cell* **166**, 1423–1435.e12 (2016).
29. G. D. Pintilie, J. Zhang, T. D. Goddard, W. Chiu, D. C. Gossard, Quantitative analysis of cryo-EM density map segmentation by watershed and scale-space filtering, and fitting of structures by alignment to regions. *J. Struct. Biol.* **170**, 427–438 (2010).
30. J. R. Swedlow, K. Hu, P. D. Andrews, D. S. Roos, J. M. Murray, Measuring tubulin content in *Toxoplasma gondii*: A comparison of laser-scanning confocal and wide-field fluorescence microscopy. *Proc. Natl. Acad. Sci. U.S.A.* **99**, 2014–2019 (2002).
31. G. Pintilie, W. Chiu, Comparison of Segger and other methods for segmentation and rigid-body docking of molecular components in cryo-EM density maps. *Biopolymers* **97**, 742–760 (2012).
32. B. Spreng *et al.*, Microtubule number and length determine cellular shape and function in *Plasmodium*. *EMBO J.* **38**, e100984 (2019).
33. J. M. Leung *et al.*, Stability and function of a putative microtubule-organizing center in the human parasite *Toxoplasma gondii*. *Mol. Biol. Cell* **28**, 1361–1378 (2017).
34. N. Tosetti *et al.*, Essential function of the alveolin network in the subpellicular microtubules and conoid assembly in *Toxoplasma gondii*. *eLife* **9**, e56635 (2020).
35. A. L. Chen *et al.*, Novel insights into the composition and function of the *Toxoplasma* IMC sutures. *Cell. Microbiol.* **19**, e12678 (2017).
36. N. J. Katris *et al.*, The apical complex provides a regulated gateway for secretion of invasion factors in *Toxoplasma*. *PLoS Pathog.* **10**, e1004074 (2014).
37. D. Zabeo *et al.*, A luminal interrupted helix in human sperm tail microtubules. *Sci. Rep.* **8**, 2727 (2018).
38. N. S. Morrisette, L. D. Sibley, Cytoskeleton of apicomplexan parasites. *Microbiol. Mol. Biol. Rev.* **66**, 21–38; table of contents (2002).
39. D. G. Russell, R. G. Burns, The polar ring of coccidian sporozoites: A unique microtubule-organizing centre. *J. Cell Sci.* **65**, 193–207 (1984).
40. M. Wallin, E. Strömberg, Cold-stable and cold-adapted microtubules. *Int. Rev. Cytol.* **157**, 1–31 (1995).
41. G. B. Witman, K. Carlson, J. Berliner, J. L. Rosenbaum, *Chlamydomonas flagella*. I. Isolation and electrophoretic analysis of microtubules, matrix, and mastigonemes. *J. Cell Biol.* **54**, 507–539 (1972).
42. E. Frixione, R. Mondragón, I. Meza, Kinematic analysis of *Toxoplasma gondii* motility. *Cell Motil. Cytoskeleton* **34**, 152–163 (1996).
43. S. Håkansson, H. Morisaki, J. Heuser, L. D. Sibley, Time-lapse video microscopy of gliding motility in *Toxoplasma gondii* reveals a novel, biphasic mechanism of cell locomotion. *Mol. Biol. Cell* **10**, 3539–3547 (1999).
44. K. Barylyuk *et al.*, A comprehensive subcellular atlas of the *Toxoplasma* proteome via hyperLOPIT provides spatial context for protein functions. *Cell Host Microbe* **28**, 752–766.e9 (2020).
45. X. Wang *et al.*, Publisher correction: Cryo-EM structure of cortical microtubules from human parasite *Toxoplasma gondii* identifies their microtubule inner proteins. *Nat. Commun.* **12**, 4076 (2021).
46. J. Q. Tran, C. Li, A. Chyan, L. Chung, N. S. Morrisette, SPM1 stabilizes subpellicular microtubules in *Toxoplasma gondii*. *Eukaryot. Cell* **11**, 206–216 (2012).
47. J. Liu *et al.*, An ensemble of specifically targeted proteins stabilizes cortical microtubules in the human parasite *Toxoplasma gondii*. *Mol. Biol. Cell* **27**, 549–571 (2016).
48. E. Nagayasu, Y.-C. Hwang, J. Liu, J. M. Murray, K. Hu, Loss of a doublecortin (DCX)-domain protein causes structural defects in a tubulin-based organelle of *Toxoplasma gondii* and impairs host-cell invasion. *Mol. Biol. Cell* **28**, 411–428 (2017).
49. F. J. Fourniol *et al.*, Template-free 13-protofilament microtubule-MAP assembly visualized at 8 Å resolution. *J. Cell Biol.* **191**, 463–470 (2010).
50. S. Bechstedt, K. Lu, G. J. Brouhard, Doublecortin recognizes the longitudinal curvature of the microtubule end and lattice. *Curr. Biol.* **24**, 2366–2375 (2014).
51. Q. S. Zheng, M. B. Braunfeld, J. W. Sedat, D. A. Agard, An improved strategy for automated electron microscopic tomography. *J. Struct. Biol.* **147**, 91–101 (2004).
52. S. Q. Zheng *et al.*, MotionCor2: Anisotropic correction of beam-induced motion for improved cryo-electron microscopy. *Nat. Methods* **14**, 331–332 (2017).
53. J. R. Kremer, D. N. Mastronarde, J. R. McIntosh, Computer visualization of three-dimensional image data using IMOD. *J. Struct. Biol.* **116**, 71–76 (1996).
54. D. N. Mastronarde, Dual-axis tomography: An approach with alignment methods that preserve resolution. *J. Struct. Biol.* **120**, 343–352 (1997).
55. E. F. Pettersen *et al.*, UCSF Chimera—A visualization system for exploratory research and analysis. *J. Comput. Chem.* **25**, 1605–1612 (2004).
56. T. I. Croll, ISOLDE: A physically realistic environment for model building into low-resolution electron-density maps. *Acta Crystallogr. D Struct. Biol.* **74**, 519–530 (2018).
57. S. Birmanns, M. Rusu, W. Wriggers, Using Sculptor and Situs for simultaneous assembly of atomic components into low-resolution shapes. *J. Struct. Biol.* **173**, 428–435 (2011).